Station-orientation catalog for Australian broadband seismic stations

Kotaro Tarumi * [1], **Kazunori Yoshizawa** [1,2]

[1]Department of Natural History Sciences, Graduate School of Science, Hokkaido University, Sapporo 060-0810, Japan., [2]Department of Earth and Planetary Sciences, Faculty of Science, Hokkaido University, Sapporo 060-0810, Japan.

Author contributions: *Conceptualization, Methodology, Formal Analysis, Investigation, Funding acquisition*: Kotaro Tarumi, Kazunori Yoshizawa. *Writing - Original draft, Software, Visualization*: Kotaro Tarumi. *Writing - Review & Editing, Supervision, Project administration*: Kazunori Yoshizawa.

Abstract Many broadband seismic stations deployed permanently and temporarily in the Australian continent have been used for various seismological investigations in and around Australia. Although two horizontal components are generally assumed to be oriented in the north and east directions, as reported by data providers, misorientations of horizontal components from the true geographic north direction cannot be avoided in practical field observations, even in the well-maintained permanent stations. In this report, we applied a polarization analysis to almost all stations in Australia to estimate the misorientations of horizontal components using long-period teleseismic P-waves. A large data set of P-wave arrival angles allows us to successfully detect probable horizontal misorientations, including significant temporal changes in some stations, which generally happened at reported timings of station maintenance and instrument replacements. However, some stations exhibit misorientations and temporal changes at unexpected timings that are unreported. Compiling the information on such time-dependent misorientations, we created a full catalog of horizontal-component orientations for both permanent and temporary stations in Australia, which are widely available for the community.

1 Introduction

A large number of broadband seismic stations deployed permanently or temporarily in the Australian continent have provided key information on seismic wave propagation (e.g., Kennett and Furumura, 2008), seismic sources (e.g., Hejrani and Tkalčić, 2020), and seismic structure (e.g., Kennett et al., 2013; Yoshizawa, 2014; Birkey and Ford, 2023; Eakin et al., 2023) in and around Australia. As an initial step for the three-component seismic waveform analysis, we generally rotate two horizontal components (e.g., NS / EW) to radial and transverse directions, supposing that the horizontal sensors are oriented in the north and east (or in reported) directions. However, as several earlier

*Corresponding author: tarumi.kotaro.jp@gmail.com

studies suggested, there is a possibility of nontrivial misorientation of horizontal components at some stations (e.g., Laske, 1995; Yoshizawa et al., 1999; Schulte-Pelkum et al., 2001). Also, temporal changes in the amplitude gain of seismometers may occur at some permanent stations over a long observation period (Ekström et al., 2006). Such errors or uncertainties in the reported catalog values, particularly the ambiguities in the horizontal-component orientation, would prevent us from performing precise waveform analyses that depend on the horizontal directions, such as shear-wave splitting measurements, Love-wave dispersion analysis, and the azimuthal dependency of receiver functions.

The horizontal orientation of seismic stations can be estimated by measuring the arrival angles of teleseismic P or Rayleigh waves at longer periods for a large number of seismic events (e.g., Laske and Masters, 1996; Yoshizawa et al., 1999; Schulte-Pelkum et al., 2001; Larson and Ekström, 2002; Ekström and Busby, 2008). Rayleigh waves generally oscillate elliptically in the radial-vertical plane, but their particle motions become more complicated in heterogeneous and anisotropic media (Crampin, 1975). Moreover, due to the dispersive nature of surface waves, the arrival-angle anomalies (or deviations from the great-circle path) depend significantly on the frequency (Laske, 1995; Yoshizawa et al., 1999), which may increase uncertainties in the estimated station orientation. Furthermore, the overlaps by preceding Love waves in the transverse component make it difficult to perform arrival-angle analysis of Rayleigh waves at relatively shorter epicentral distances of less than 50° (Yoshizawa et al., 1999). On the contrary, the onset of teleseismic P-waves exhibits a relatively simple linear motion in the radial-vertical plane without frequency dependence. Teleseismic P waves with the near-vertical incidence to the station mainly sample the lower mantle where lateral heterogeneities are weak. Thus, the ray-bending effects on P-waves due to strong lateral heterogeneity in the upper mantle can be milder than that on surface waves (Yoshizawa et al., 1999), in addition to the relatively smaller influence from anisotropy on P-waves compared to surface waves (Crampin et al., 1982).

Recently, major seismological data centers, such as IRIS (Incorporated Research Institutions for Seismology), have provided us with more precise information on the station orientation for their affiliated stations worldwide, including Australian stations. Given proper information from careful calibrations, many of the broadband horizontal channels in major stations in global networks (such as the Global Seismograph Network) have been named BH1 and BH2 (for the first and second components) rather than conventional BHN and BHE (North and East), when the true horizontal directions deviate from the geographic north and east (Ekström and Busby, 2008). Ekström (2008) has also provided practically useful tables on the station orientation for GSN stations until 2015. However, a number of seismic stations from local data providers and temporary seismic networks, including transportable seismic arrays (e.g., SKIPPY in Australia; Hilst et al., 1994), still lack precise information on horizontal orientations, which is crucial for researchers wishing to utilize these valuable waveform data sets.

In this report, we collect a large number of P-wave arrival angle data to estimate the horizontal orientation of many broadband seismic stations in Australia, modeled on the method of polarization analysis by Vidale (1986) utilized in earlier study by Yoshizawa et al. (1999). Through the polarization analysis of teleseismic P-wave particle motions, we construct a complete catalog of the horizontal orientation of currently available broadband stations in Australia, which can be used for a variety of future applications of seismic data analyses with horizontal components.

2 Data and Method

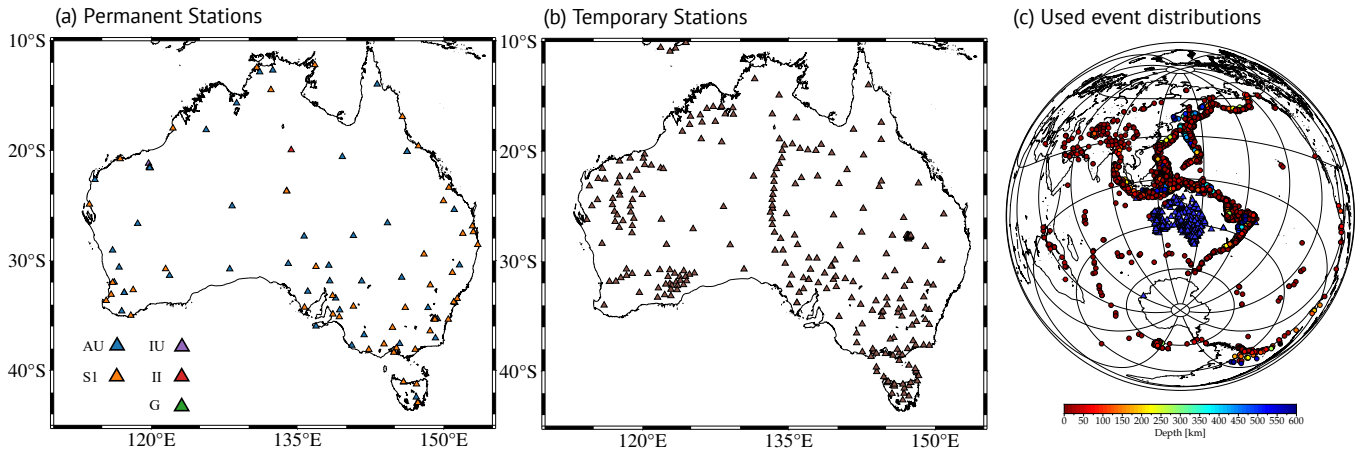

Figure 1 Broadband seismic stations and seismic events used in this study. (a) Permanent stations, with colors indicating different networks (AU, S1, IU, II, and G). (b) Temporary stations. (c) Seismic events used in this study, with colors representing source depths. Blue triangles are employed stations in (a) and (b).

We used the three-component teleseismic P-wave data downloaded from the IRIS Data Management Center (IRIS DMC) and Australian Passive Seismic Server (AusPass) for 4004 seismic events with moment magnitude Mw $\geq$ 5.5 from 1987 to 2019. Our dataset includes both permanent and temporary broadband stations shown in Figures 1 (a, b). Permanent seismic networks include IRIS/IDA (red triangles in Figure 1 (a); Network II), IRIS/USGS (purple triangles in Figure 1 (a); Network IU), GEOSCOPE (green triangles in Figure 1 (a); Network G), GeoScience Australia (blue triangles in Figure 1 (a); Network AU), and Australian Seismometers in Schools program (orange triangles in Figure 1 (a); Network S1). Temporary stations shown in Figure 1 (b) involve many temporary seismic arrays, SKIPPY (Hilst and Kennett, 1993), KIMBA (Kennett, 1997, 1998), QUOLL (Kennett et al., 1999), West Australia Cratons Kennet (2000), TRIGGER BB (Rawlinson and Kennett, 2001), TASMAL (Kennett, 2003), CARPA - Linkage (Reading and Kennett, 2005), SOC - Southern Craton (Fontaine and Kennet, 2007), BILBY (Rawlinson and Kennet, 2008), Bass Strait (Reading and Rawlinson, 2011), Australia (Tkalčić et al., 2013b), Albany-Fraser Experiment (Tkalčić et al., 2013a), and Transitions in the Banda Arc-Australia continental collision (Miller, 2014).

We selected seismic events with Mw $\geq$ 5.5, distance ranges between 30 and 90 degrees, and normalized amplitude of P-wave radiation $> |0.3|$ estimated from the Global CMT catalog (Dziewonski et al., 1981; Ekström et al., 2012). We first corrected the instrument response, converted the waveform data into the displacement, and applied a band-pass filter between 0.03 and 0.1 Hz. Second, we rotated the two horizontal waveforms into the radial and transverse components based on the station catalog information of horizontal orientation provided by IRIS DMC and AusPass. To discard the low-quality data, we calculated signal-to-noise ratios (SNR) in the vertical and radial components and removed data with vertical SNR < 5.0 or radial SNR < 3.0. Then, for each seismic event and station, we performed a time-domain complex polarization analysis of Vidale (1986) to measure the horizontal arrival angles Θ of direct P-waves in a similar way to Yoshizawa et al. (1999), which is summarized in Figure 2. Since teleseismic P-wave is likely to linearly oscillate in the radial-vertical plane, we imposed the data selection criteria on the ellipticity parameter P_E smaller than 0.175. Third, we calculated the median of the time-dependent arrival angles for each event (an orange line in the third panel in Figure 2 (a)) in a selected time window. In this study, we set the time window as 7.5 s before

and after the main P-wave pulse (Figure 2 (a)). Consequently, in the final step, we compiled a large number of arrival angle data from many seismic events to evaluate the misorientation of horizontal sensors. In this study, to reduce the influence of biased event distributions, we mainly adopted the median as a representative measure for arrival-angle anomalies (i.e., deviations from the great-circle direction) over the selected observation period (Figure 2 (b)). Still, we also reported the mean values in our catalog (Tables S1–S3 and Tarumi and Yoshizawa (2024)). We conducted this final step for stations with more than 5 arrival-angle measurements, and discarded several stations with large uncertainties in the time-dependent polarization data via visual inspections. The resultant distribution of all employed events used in this study is shown in Figure 1 (c).

Station metadata (or reported catalog information of horizontal orientation) for permanent stations is subject to change from time to time, reflecting irregular maintenance, calibrations, and replacement of instruments. For the permanent stations with a long observation period, we visually inspected the timing of sudden changes in the trend of estimated horizontal misorientation, allowing us to detect some temporal changes at unreported timings (e.g., AU.COEN in Figure 3 (f)). For the estimation of horizontal misorientation, we divide the period windows in which the median of measured arrival angles is computed, depending on each station, as shown in Figures 2 (b) and 3.

3 Results

Our arrival-angle measurements enabled us to detect probable misorientations from the geographic north for permanent and temporary stations (Figures 2, 3, 4, 5, and S7). All results are summarized in Supplementary Materials 2 (Tables S1–S3) and Zenodo Repositiory (Tarumi and Yoshizawa, 2024). In this section, we explain our results on the permanent and temporary stations separately.

3.1 Permanent Stations

Figure 2 shows the summary of P-wave polarization measurements for IU.NWAO which has been a long-running station located in southeast Australia since 1992. According to the IRIS metadata catalog, the channel name of the horizontal components was changed from BHN/BHE to BH1/BH2 in September 2001. Our measured P-wave arrival angles show apparent temporal changes in the polarization trend at this time. The misorientation angle of horizontal sensors was estimated to be about 5.8° before September 2001, and it has decreased to 0.6° since then (by 2019, at least), indicating the improvement in the catalog information of this station.

Note that, for this station, Laske and Masters (1996), Yoshizawa et al. (1999), and Schulte-Pelkum et al. (2001), who employed the particle motion of either Rayleigh wave or teleseismic P-wave before 2000, have already reported the misalignment from the north by around 5°. In particular, our estimated misorientation angle (5.8°) before September 2001 in Figure 2 (b) is very close to the estimated value by Schulte-Pelkum et al. (2001), who employed the P wave data in the same period. Fontaine et al. (2009) also used similar P-wave datasets and identified a misalignment of 5°, which is consistent with our results. For the other GSN stations used in this study, our estimated orientations are generally in agreement with the previously published catalog (Ekström, 2008).

In addition to temporal changes, we can also see a back-azimuthal dependence in the arrival-angle data (Figure 2 (b, bottom-right panel)). Such azimuthal variations of arrival angles can also be observed at other stations, which may be worth further investigation in the future since they may reflect the lateral variations of heterogeneity and

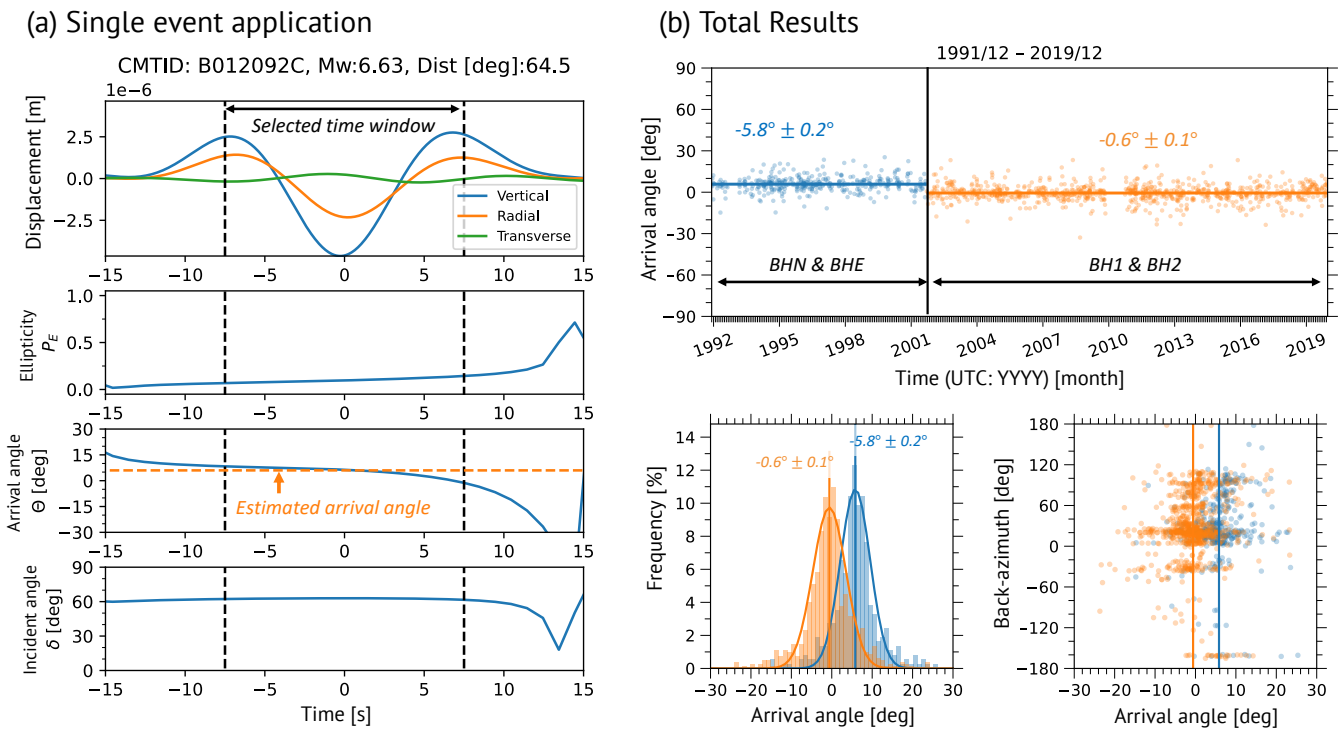

Figure 2 A visual summary of P-wave polarization analysis for IU.NWAO. (a) An example of teleseismic P-wave for an event at the epicentral distance of 64.5 degrees and the estimated polarization parameters. From top to bottom: three-component displacement waveforms rotated to the catalog values of IRIS metadata (blue: vertical; orange: radial; green: transverse), ellipticity P_E, arrival angle Θ on a horizontal plane, and incident angle δ for the P-wave particle motion. The arrival angle is measured clockwise from the radial (great-circle) direction so that a positive deviation indicates the arrival-angle anomaly to the east. In the third panel, a dashed orange line exhibits a median value in the selected time window encompassed by vertical dashed lines. (b) Compiled P-wave polarization data for all events used for the NWAO station. The top panel represents the time series of P-wave arrival angles. The colors for dots and lines represent the distinct period characterized by different trends of arrival angles. The timing of the arrival-angle trend change in September 2001 (indicated by a solid vertical line) matched well with the reported correction of horizontal components by IRIS. The bottom-left panel shows histograms and fitted Gaussian function for each period, and the bottom-right one indicates the back-azimuth dependence of the measured arrival angles for all employed events. In the top and bottom-left panels, the estimated station orientations and standard errors are labeled. The colors of the characters correspond to each distinct time period.

azimuthal anisotropy, including dipping interfaces, in the upper mantle beneath the seismic station (Schulte-Pelkum et al., 2001; Fontaine et al., 2009).

Figure 3 shows the summary of P-wave polarization data (arrival-angle anomalies from the great circle for each path) for six permanent and two temporary stations during their operation period until 2019. The horizontal-component channels of these stations have been reported as BHN/BHE since their installation. At G.CAN (Canberra by GEOSCOPE; Figure 3 (a)), the station orientation estimated in this study is nearly 0° (Tables S1–S3 in Supplementary Materials), suggesting that this seismometer has been accurately oriented to the geographic north and east. AU.TOO (Figure 3 (b)) also shows no significant temporal changes, though our measurements suggest a slight misalignment (about -1.2°) from the north which can be almost negligible. At AU.BBOO and AU.KMBL stations (Figure 3 (c, d)), we can see clear temporal changes in the trends of polarization angles, which coincide well with the timing of reported maintenance and/or instrument replacement. On the other hand, at AU.STKA and AU.COEN (Figure 3 (e, f)), unknown temporal changes in polarization angles are detected at unreported timings. In particular, STKA exhibits a very large misalignment from the north by 30° since the early stage of its operation.

Compiled maps of the estimated horizontal misorientations for permanent stations are displayed in Figure 4, in

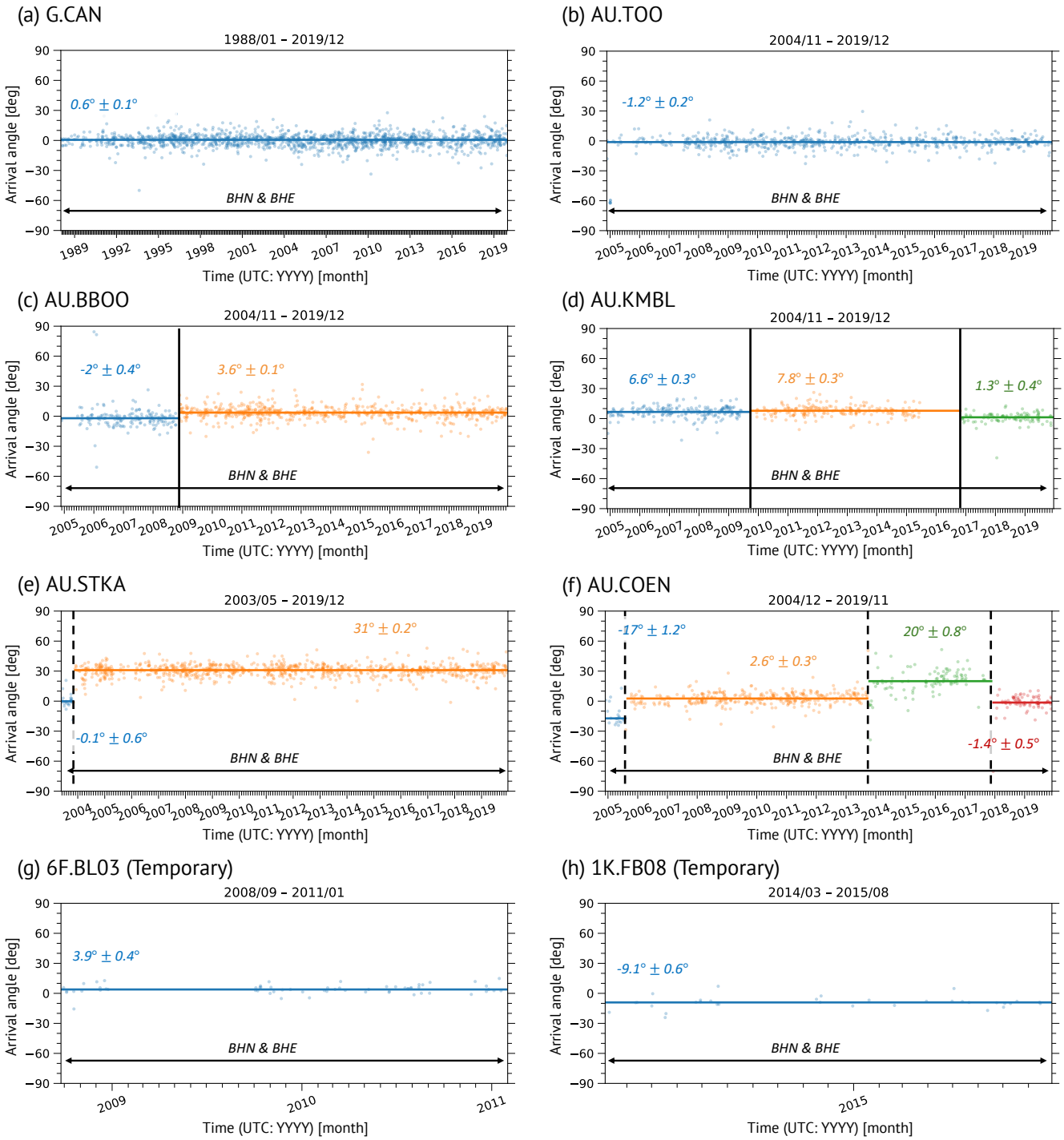

Figure 3 Time-dependent P-wave polarization data (arrival-angle deviation from the great circle) for selected stations, (a-f) permanent stations installed and maintained by GEOSCOPE (G) and Geoscience Australia (AU), and (g, h) temporary stations. Notations in these figures are the same as 2 (b, top panel). The vertical black lines represent the timing of significant trend changes in P-wave arrival angles. Solid vertical lines indicate the timing of the reported maintenance and/or replacement of instruments, and dashed vertical lines represent unknown temporal changes at unreported timings. As described in the main text, we did not identify temporal change for temporary stations.

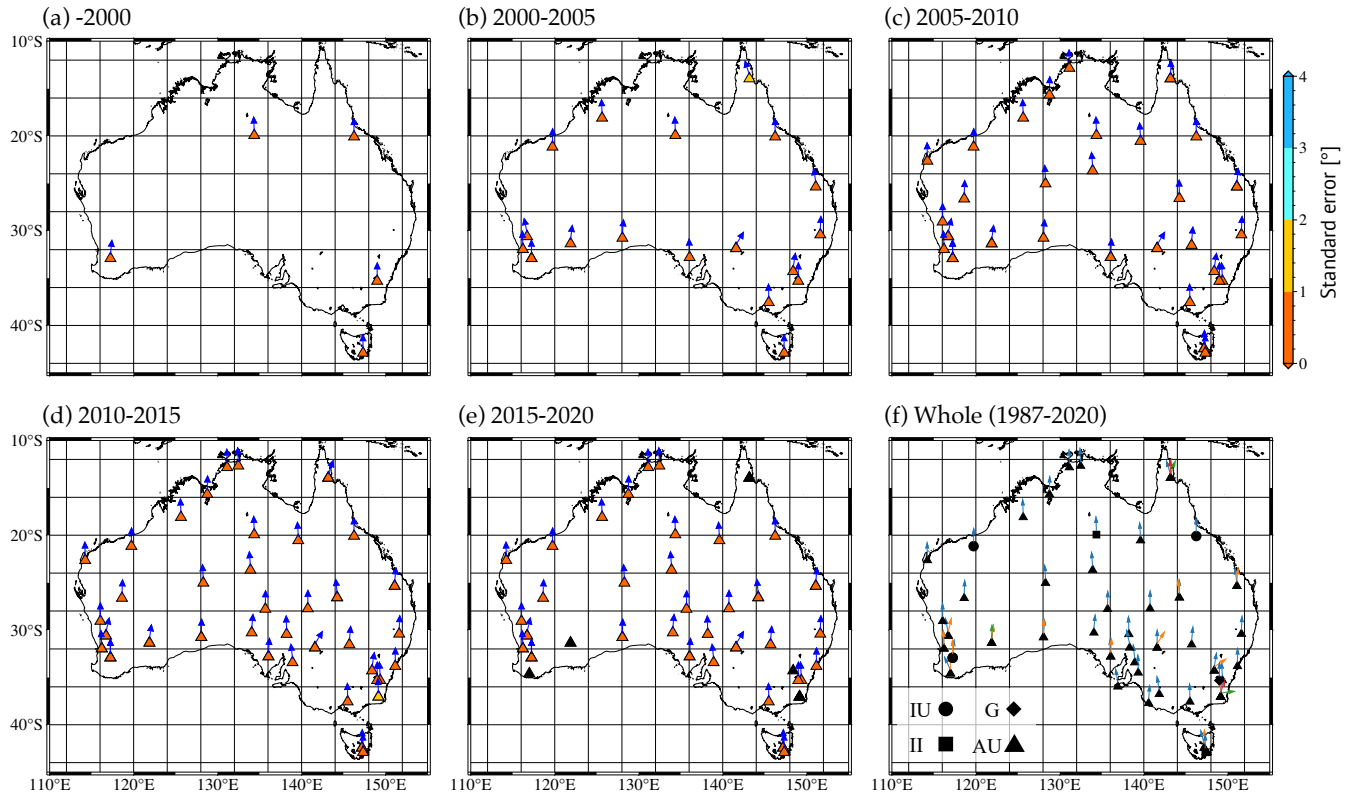

Figure 4 Map projections of horizontal misorientations from the geographic north for permanent seismic stations (II, IU, G, and AU) in Australia. (a-e) Arrows indicate the median directions of horizontal sensors over the designated period. Colors in the triangles indicate the estimated standard errors shown in the color bar on the right. Black triangles without arrows indicate stations with varying misorientations during the period. (f) A compiled map of estimated misorientations for the whole period of analysis. The colors of arrows indicate the horizontal sensor orientations in different periods. Black symbols indicate stations of different seismic networks.

which we show the misorientations in each period in Figures 4 (a-e), and those compiled for the entire period of our analysis in Figure 4 (f). For permanent stations including those in the S1 network, the station misorientations and their standard errors are summarized in time-dependent horizontal bar graphs in Figures S1, S2, and S5 in Supplementary Material 1 (hereafter SM1) and are separately tabulated in Tables S1 and S2 in Supplementary Material 2 (hereafter SM2). In particular, we can identify significant time-dependent variations of misorientations for AU stations. These temporal changes mostly coincide with the reported timing of maintenance and/or replacement by the IRIS and AusPass. However, such temporal changes at several stations (e.g., AU.COEN) are found at unreported timings. The misorientation of some permanent stations from the geographic north is more than 10°, which may affect seismic waveform analysis, especially when using the horizontal components. Figure S6 (SM1) demonstrates the three-component seismograms observed at STKA to compare waveforms before and after correcting the station misorientations. In Figure S6 (a) in SM1, we can see the apparent energy leakage of the P-wave from the radial to transverse component. In Section 4, we will discuss the effects of the station correction on azimuth-dependent receiver function analyses.

For AU stations, we compare our measurements with those from a recent study in Table 1; we present our estimated misalignments for selected AU stations, along with XKS-based measurements from Eakin et al. (2023). We focused on stations where Eakin et al. (2023) reported non-zero misalignments and extracted the most recent misorientation data from our catalog between 1987 and 2019 for comparison. Our measurements are generally in good

Table 1 Comparison of recent misalignment measurements at AU stations by Eakin et al. (2023) and this study. Eakin et al. (2023) estimated these using PKS and/or SKS phases, as indicated. In the third column showing our results, the data period and the number of seismic events used are shown (e.g., 2011–2019; 100).

Station	Eakin et al. (2023) (PKS and/or SKS)	This study (Teleseismic P-wave)
AU.ARPS	-6° (SKS)	-9.4°±4.4° (2019; 6)
AU.FORT	0° (PKS), 3.5° (SKS)	4.4°±0.4° (2003–2011; 69) 1.4°±0.2° (2011–2019; 404)
AU.HTT	-4° (PKS), -3° (SKS)	-6.3°±0.2° (2010-2019; 399)
AU.KELC	-6° (SKS)	-9°±1.3° (2019; 19)
AU.MGBR	-10° (SKS)	4.4°±1.8° (2019; 30)
AU.MILA	6° (SKS)	1.7°±0.6° (2011–2014; 44) -2.5°±1.6° (2014–2016; 22) 83°±0.9° (2016–2018; 18) 17°±1.1° (2018–2019; 17) 6.5°±1.0° (2019; 12)
AU.MULG	6.6° (PKS & SKS)	5.0°±0.4° (2013–2019; 219)
AU.SDAN	2.5° (SKS)	-1.5°±0.7° (2018–2019; 48)
AU.STKA	31° (PKS & SKS)	-0.1°±0.6° (2003; 23) 31.0°±0.2° (2003–2019; 899)
AU.YAPP	-13.4° (PKS & SKS)	-13°±0.5° (2018–2019; 55)
AU.YNG	5° (PKS), 10° (SKS)	8.7°±0.3° (2004–2017; 429) 56°±1.2° (2004–2017; 42)

agreement with those of Eakin et al. (2023). Note that large misalignments at AU.STKA are identical between both studies.

Figure S7 shows the map of station orientations for the S1 network (broadband seismometers in schools; Balfour et al., 2014), which has been installed since 2011 (Salmon et al., 2011). Table S2 in Supplementary Material 2 lists the estimated station orientations and their standard errors. Note that the lower corner-frequency of seismometers (Güralp CMG-6TD) used for the S1 network (Balfour et al., 2014) is relatively high (0.03Hz) compared to other permanent networks. Although we could obtain many high-quality arrival-angle data when analyzing waveforms in the higher-frequency range (e.g., 0.1–1.0 Hz), we could not gather sufficient arrival-angle measurements to evaluate the station orientation for half of the S1 network since our current analysis focuses on longer-period datasets (0.03–0.1 Hz). As a result, our S1 network catalog (Table S2) includes only 13 stations (Figures S5 and S8).

3.2 Temporary Stations

The seismic records of temporary stations are generally less than two years long, and we could not find any significant temporal changes in the horizontal orientation. Figures 3 (g) and (h) show examples of a time-dependent polarization measurement for selected temporary stations. As expected from the limited data acquisition period, we could not observe any significant temporal changes in the time-series data of these stations. In Figure 5, we compiled the station orientation for all temporary stations that met the criteria described in Section 2. Also, we summarized the station orientations and their standard errors in Figures S3 and S4 and Table S3 in Supplemental Materials. While some stations exhibit relatively large misalignments, the horizontal sensors at almost all temporary stations generally align with the geographic north and east directions (Figures 5 and S3), suggesting proper installation. We also compare XKS-based measurements from Eakin et al. (2023) and teleseismic P-wave measurements from this study in Table 2, similar to the previous subsection. Overall, for most temporary stations, our results are generally consistent with those of Eakin et al. (2023). The discrepancies at some stations may be attributed to the utilized recording periods,

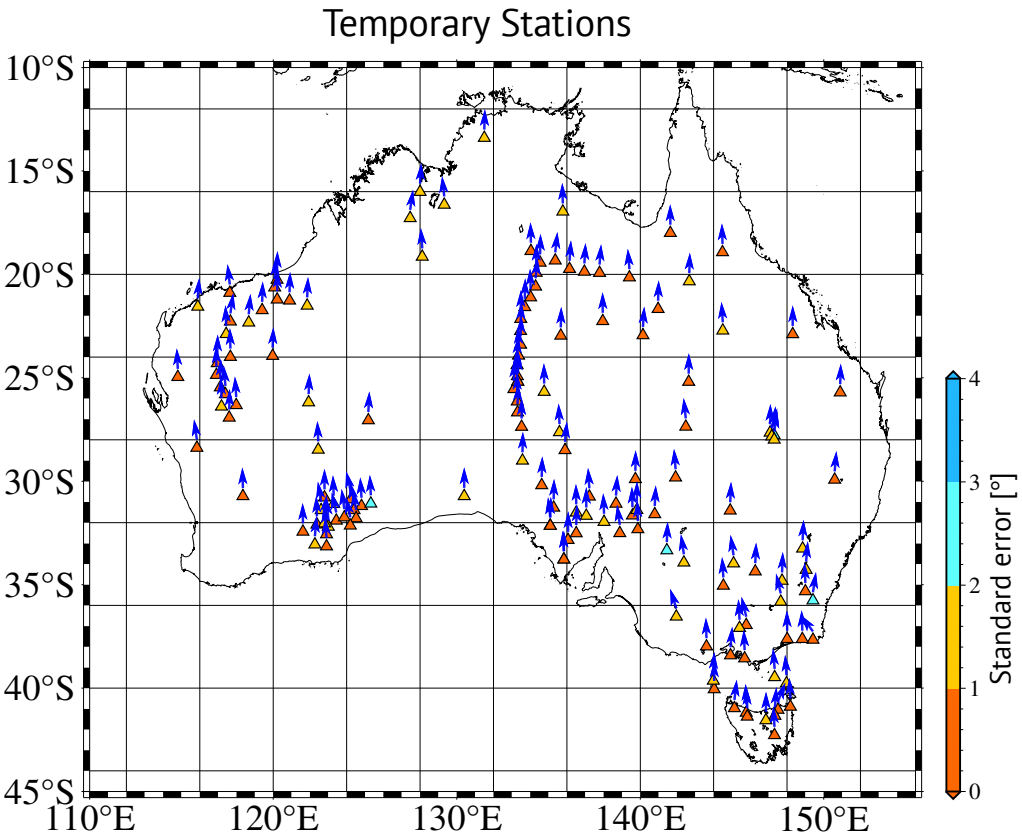

Figure 5 Station misorientations from the geographic north in a horizontal sensor for temporary seismic stations.

the measurement quality for different seismic phases, and the number of employed events.

4 Discussion and Conclusions

In this section, we briefly examine the effect of the station correction on P-wave receiver function (P-RF) analysis. We computed the P-RFs at AU.STKA, where a large misorientation of over 30° was observed, and analyzed the differences between uncorrected and corrected P-RF data for both radial and transverse components. In these calculations, we considered the azimuthal dependence of P-RFs, which arises from the varying incoming directions (or back-azimuths) of teleseismic P-wave. The azimuth-dependent radial P-RFs reflect lateral variations in seismic dis-

Table 2 Same as Table 1, but for selected temporary stations.

Station	Eakin et al. (2023) (PKS and/or SKS)	This study (Teleseismic P-wave)
1E.SQA01	5° (SKS)	3.0°±2.4° (2013–2014; 7)
1E.SQA09	10° (SKS)	16.0°±1.4° (2013–2014; 7)
1E.SQA11	10° (SKS)	9.2°±1.3° (2013–2014; 7)
1P.BA12	-25° (SKS)	-36.0°±0.9° (2011-2013; 9)
1P.BA13	0° (SKS)	-1.8°±0.8° (2011–2013; 26)
1P.BA19	9° (SKS)	-2.7°±0.8° (2011–2013; 16)
7H.TB03	5° (SKS)	-3.0°±1.0° (2011-2013)
7I.GA06	-5° (PKS), 0° (SKS)	-6.3°±0.9° (2004; 7)
7I.GA08	-5° (SKS)	-3.4°±0.9° (2004–2005; 10)
7I.TL10	-7° (PKS & SKS)	-6.1°±0.8° (2003–2005; 19)
7I.TL14	0° (PKS), 8° (SKS)	-4.4°±0.7° (2003–2005; 38)
7I.TL17	5° (SKS)	-1.4°±0.4° (2003–2005; 30)
7K.SOC03	0° (PKS), 5° (SKS)	2.7°±1.26° (2007–2008; 6)

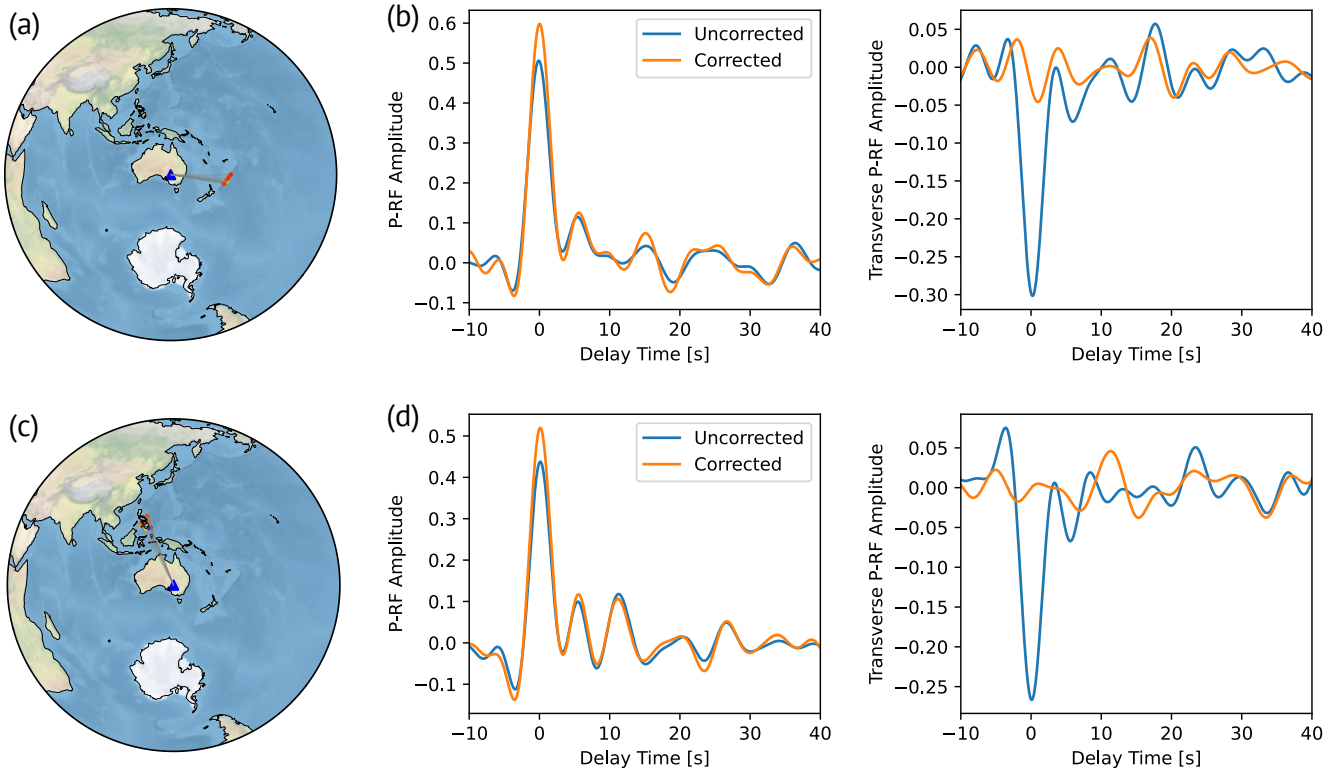

Figure 6 Comparison of P-wave receiver functions (P-RFs) for AU.STKA. (a, c) Maps showing event groups used for the P-RF analysis. (b) Stacked radial and transverse P-RFs for the eastern events shown in (a). Blue and orange lines represent P-RFs from uncorrected and corrected teleseismic P-wave data, respectively. (d) Same as (b), but for the northwestern events shown in (c).

continuities around the station (e.g., Tonegawa et al., 2005; Kawakatsu et al., 2009; Kumar and Kawakatsu, 2011). In addition, incorporating transverse P-RFs enables us to infer seismic anisotropy in the crust and upper mantle (e.g., Park and Levin, 2016; Shiomi, 2017; Birkey and Ford, 2023). Significant uncertainties in the horizontal component orientations could lead to misinterpretations in the results of P-RF analysis.

Figure S6 in Supplementary Material 1 shows an example of teleseismic P-wave records observed at AU.STKA before and after the correction for station orientation, clearly indicating the energy leakage of P-wave from radial to transverse in the uncorrected horizontal traces. Using these two sets of teleseismic P-wave data, we computed radial and transverse P-RFs for two incoming directions within narrow distance ranges (10°) (Figure 6 (a, c)). After calculating individual P-RFs, we selected P-RF traces using the cross-correlation coefficient (CC)-based selection method (Tkalčić et al., 2011), stacking all traces with CC > 0.7. The resulting stacked P-RF traces are shown in Figure 6 (b, d), and the stacking process is visually summarized in Figures S8 and S9 in Supplementary Material 1. The radial P-RFs are generally consistent regardless of the correction of misorientation. Still, the relative amplitude of converted phases for the direct P-wave can be modulated, potentially affecting analyses that rely on RF amplitude. For the transverse RFs, clear differences emerge between the uncorrected and corrected P-RF traces. In the uncorrected transverse P-RFs, we can see clear signals of direct P-wave, Moho-converted phases, and their multiple reflections, contaminating the P-to-SH converted phases. This contamination prevents us from properly interpreting P-to-SH conversions, which can be generated by anisotropic properties or oblique interfaces. Therefore, proper corrections of station azimuths during the waveform processing are essential for the accurate interpretation of both radial and

transverse P-RF amplitudes.

In this study, we constructed a comprehensive station orientation catalog for Australian broadband seismic stations by analyzing long-period teleseismic P-wave particle motion data. The catalog includes temporal variations in station misorientations. While the timing of these changes is generally consistent with the published IRIS catalog, some stations exhibit changes at unexpected times. Finally, we assessed the utility of our catalog in receiver function analysis, demonstrating that correcting for station misorientation can significantly affect the amplitude analysis of RFs, particularly in the transverse component.

Acknowledgements

All seismograms used in this study were downloaded from the IRIS Data Management Center (https://ds.iris.edu/ds/nodes/dmc/ and the Australian Passive Seismic Server (AusPass; https://auspass.edu.au/index.html). We also acknowledge Geoscience Australia for providing the AU network data. We appreciate Göran Ekström for the dissemination of his comprehensive station orientation catalog (Ekström, 2008), which was extremely useful for validating our results. This study was partially supported by the JST SPRING grant number JPMJSP2119 to KT, JSPS KAKENHI grand number 24KJ0294 to KT, and JSPS KAKENHI grant numbers 20K04096 and 23K03539 to KY. We used ObsPy (Beyreuther et al., 2010) for seismic waveform analysis and data retrieval. Figures in this paper were generated using matplotlib (Hunter, 2007), cartopy (Met Office, 2010), Generic Mapping Tools (Wessel et al., 2019), and PyGMT (Uieda et al., 2021). The earthquake catalogs utilized in this study were derived from Global CMT (Dziewonski et al., 1981; Ekström et al., 2012).

Data and code availability

The numerical data of our station misorientation catalog are included in PDF files provided as a part of Supplementary Materials and Zenodo Repository (Tarumi and Yoshizawa, 2024). The data analysis code used in this study can be available upon request. All teleseismic waveform data used in this study are available from the IRIS Data Management Center (https://ds.iris.edu/ds/nodes/dmc/) and the Australian Passive Seismic Server (AusPass; https://auspass.edu.au/index.htm

Competing interests

The authors declare that they have no known competing financial interests or personal relationships that could have appeared to influence the work reported in this paper.

References

Balfour, N. J., Salmon, M., and Sambridge, M. The Australian Seismometers in Schools Network: Education, Outreach, Research, and Monitoring. *Seismological Research Letters*, 85(5):1063–1068, 2014. doi: 10.1785/0220140025.

Beyreuther, M., Barsch, R., Krischer, L., Megies, T., Behr, Y., and Wassermann, J. ObsPy: A Python Toolbox for Seismology. *Seismological Research Letters*, 81(3):530–533, 2010. doi: 10.1785/gssrl.81.3.530.

Birkey, A. and Ford, H. A. Anisotropic structure of the Australian continent. *Frontiers in Earth Science*, 10:1055480, 2023. doi: 10.3389/feart.2022.1055480.

Crampin, S. Distinctive Particle Motion of Surface Waves as a Diagnostic of Anisotropic Layering. *Geophysical Journal of the Royal Astronomical Society*, 40(2):177 – 186, 00 1975. doi: 10.1111/j.1365-246x.1975.tb07045.x.

Crampin, S., Stephen, R. A., and McGonigle, R. The polarization of P-waves in anisotropic media. *Geophysical Journal of the Royal Astronomical Society*, 68(2):477–485, 00 1982. doi: 10.1111/j.1365-246x.1982.tb04910.x.

Dziewonski, A. M., Chou, T., and Woodhouse, J. H. Determination of earthquake source parameters from waveform data for studies of global and regional seismicity. *Journal of Geophysical Research: Solid Earth*, 86(B4):2825–2852, 1981. doi: 10.1029/jb086ib04p02825.

Eakin, C. M., Davies, D. R., Ghelichkhan, S., O'Donnell, J. P., and Agrawal, S. The Influence of Lithospheric Thickness Variations Beneath Australia on Seismic Anisotropy and Mantle Flow. *Geochemistry, Geophysics, Geosystems*, 24(9), 2023. doi: 10.1029/2023gc011066.

Ekström, G. Polarization anomalies at various stations, 2008. https://www.ldeo.columbia.edu/~ekstrom/Projects/WQC/COMB_QC/.

Ekström, G. and Busby, R. W. Measurements of Seismometer Orientation at USArray Transportable Array and Backbone Stations. *Seismological Research Letters*, 79(4):554–561, 2008. doi: 10.1785/gssrl.79.4.554.

Ekström, G., Dalton, C. A., and Nettles, M. Observations of Time-dependent Errors in Long-period Instrument Gain at Global Seismic Stations. *Seismological Research Letters*, 77(1):12–22, 2006. doi: 10.1785/gssrl.77.1.12.

Ekström, G., Nettles, M., and Dziewoński, A. The global CMT project 2004–2010: Centroid-moment tensors for 13,017 earthquakes. *Physics of the Earth and Planetary Interiors*, 200:1–9, 2012. doi: 10.1016/j.pepi.2012.04.002.

Fontaine, F. and Kennet, B. SOC - Southern Craton, 2007. https://www.fdsn.org/networks/detail/7K_2007/.

Fontaine, F. R., Barruol, G., Kennett, B. L. N., Bokelmann, G. H. R., and Reymond, D. Upper mantle anisotropy beneath Australia and Tahiti from P wave polarization: Implications for real-time earthquake location. *Journal of Geophysical Research: Solid Earth*, 114(B3), 2009. doi: 10.1029/2008jb005709.

Hejrani, B. and Tkalčić, H. Resolvability of the Centroid-Moment-Tensors for Shallow Seismic Sources and Improvements From Modeling High-Frequency Waveforms. *Journal of Geophysical Research: Solid Earth*, 125(7), 2020. doi: 10.1029/2020jb019643.

Hilst, R. v. d. and Kennett, B. SKIPPY, 1993. https://www.fdsn.org/networks/detail/7B_1993/.

Hilst, R. v. d., Kennett, B., Christie, D., and Grant, J. Project Skippy explores lithosphere and mantle beneath Australia. *Eos, Transactions American Geophysical Union*, 75(15):177–181, 1994. doi: 10.1029/94eo00857.

Hunter, J. D. Matplotlib: A 2D Graphics Environment. *Computing in Science & Engineering*, 9(3):90–95, 2007. doi: 10.1109/mcse.2007.55.

Kawakatsu, H., Kumar, P., Takei, Y., Shinohara, M., Kanazawa, T., Araki, E., and Suyehiro, K. Seismic Evidence for Sharp Lithosphere-Asthenosphere Boundaries of Oceanic Plates. *Science*, 324(5926):499–502, 2009. doi: 10.1126/science.1169499.

Kennet, B. West Australian Cratons, 2000. https://www.fdsn.org/networks/detail/7G_2000/.

Kennett, B. KIMBA97, 1997. https://www.fdsn.org/networks/detail/7D_1997/.

Kennett, B. KIMBA98, 1998. https://www.fdsn.org/networks/detail/7E_1998/.

Kennett, B. TASMAL, 2003. https://www.fdsn.org/networks/detail/7I_2003/.

Kennett, B., Debayle, E., and Gorbatov, A. QUOLL, 1999. https://www.fdsn.org/networks/detail/7F_1999/.

Kennett, B. L. N. and Furumura, T. Stochastic waveguide in the lithosphere: Indonesian subduction zone to Australian craton. *Geophysical Journal International*, 172(1):363 – 382, 01 2008. doi: 10.1111/j.1365-246x.2007.03647.x.

Kennett, B. L. N., Fichtner, A., Fishwick, S., and Yoshizawa, K. Australian Seismological Reference Model (AuSREM): mantle component. *Geophysical Journal International*, 192(2):871–887, 02 2013. doi: 10.1093/gji/ggs065.

Kumar, P. and Kawakatsu, H. Imaging the seismic lithosphere-asthenosphere boundary of the oceanic plate. *Geochemistry, Geophysics,*

Geosystems, 12(1):n/a–n/a, 2011. doi: 10.1029/2010gc003358.

Larson, E. W. F. and Ekström, G. Determining surface wave arrival angle anomalies. *Journal of Geophysical Research*, 107(B6), 00 2002. doi: 10.1029/2000jb000048.

Laske, G. Global observation of off-great-circle propagation of Long-Period surface waves. *Geophysical Journal International*, 123(1):245 – 259, 10 1995. doi: 10.1111/j.1365-246x.1995.tb06673.x.

Laske, G. and Masters, G. Constraints on global phase velocity maps from long-period polarization data. *Journal of Geophysical Research: Solid Earth*, 101(B7):16059–16075, 1996. doi: 10.1029/96jb00526.

Met Office. *Cartopy: a cartographic python library with a Matplotlib interface*, 2010. https://scitools.org.uk/cartopy.

Miller, M. S. Transitions in the Banda Arc-Australia continental collision, 2014. https://www.fdsn.org/networks/detail/1G_2019/.

Park, J. and Levin, V. Anisotropic shear zones revealed by backazimuthal harmonics of teleseismic receiver functions. *Geophysical Journal International*, 207(2):1216–1243, 2016. doi: 10.1093/gji/ggw323.

Rawlinson, N. and Kennett, B. TIGGER BB, 2001. https://www.fdsn.org/networks/detail/7H_2001/.

Rawlinson, S. and Kennet, B. BILBY, 2008. https://www.fdsn.org/networks/detail/6F_2008/.

Reading, A. and Kennett, B. CAPRA - Linkage, 2005. https://www.fdsn.org/networks/detail/7J_2005/.

Reading, A. and Rawlinson, N. Bass Strait, 2011. https://www.fdsn.org/networks/detail/1P_2011/.

Salmon, M., Balfour, N., and Sambridge, M. Australian Seismometers in Schools, 2011. https://www.fdsn.org/networks/detail/S1/.

Schulte-Pelkum, V., Masters, G., and Shearer, P. M. Upper mantle anisotropy from long-period P polarization. *Journal of Geophysical Research: Solid Earth*, 106(B10):21917–21934, 2001. doi: 10.1029/2001jb000346.

Shiomi, K. Dissimilar receiver functions observed at very close stations in the Kii Peninsula, central Japan: features and causes. *Earth, Planets and Space*, 69(1):48, 2017. doi: 10.1186/s40623-017-0631-5.

Tarumi, K. and Yoshizawa, K. Numerical Sheet for "Station-orientation catalog for Australian broadband seismic stations", 2024. https://doi.org/10.5281/zenodo.13985090.

Tkalčić, H., Chen, Y., Liu, R., Zhibin, H., Sun, L., and Chan, W. Multistep modelling of teleseismic receiver functions combined with constraints from seismic tomography: crustal structure beneath southeast China. *Geophysical Journal International*, 187(1):303–326, 2011. doi: 10.1111/j.1365-246x.2011.05132.x.

Tkalčić, H., Kennett, B., Sippl, C., Spaggiari, C., and Gessner, K. Albany-Fraser Experiment, 2013a. https://www.fdsn.org/networks/detail/1K_2013/.

Tkalčić, H., Kennett, B., Tanaka, S., and Stipčević, J. Australia, 2013b. https://www.fdsn.org/networks/detail/1E_2013/.

Tonegawa, T., Hirahara, K., and Shibutani, T. Detailed structure of the upper mantle discontinuities around the Japan subduction zone imaged by receiver function analyses. *Earth, Planets and Space*, 57(1):5–14, 03 2005. doi: 10.1186/bf03351801.

Uieda, L., Tian, D., Leong, W. J., Jones, M., Schlitzer, W., Toney, L., Grund, M., Yao, J., Magen, Y., Materna, K., Newton, T., Anant, A., Ziebarth, M., Wessel, P., and Quinn, J. PyGMT: A Python interface for the Generic Mapping Tools. 2021. doi: 10.5281/zenodo.5607255.

Vidale, J. E. Complex polarization analysis of particle motion. *Bulletin of the Seismological Society of America*, 76(5):1393–1405, 1986. doi: 10.1785/bssa0760051393.

Wessel, P., Luis, J. F., Uieda, L., Scharroo, R., Wobbe, F., Smith, W. H. F., and Tian, D. The Generic Mapping Tools Version 6. *Geochemistry, Geophysics, Geosystems*, 20(11):5556–5564, 2019. doi: 10.1029/2019gc008515.

Yoshizawa, K. Radially anisotropic 3-D shear wave structure of the Australian lithosphere and asthenosphere from multi-mode surface

313 waves. *Physics of the Earth and Planetary Interiors*, 235:33–48, 2014. doi: 10.1016/j.pepi.2014.07.008.

314 Yoshizawa, K., Yomogida, K., and Tsuboi, S. Resolving power of surface wave polarization data for higher-order heterogeneities. *Geophysical*

315 *Journal International*, 138(1):205–220, 1999. doi: 10.1046/j.1365-246x.1999.00861.x.

Supplementary Material 1 for

Station-orientation catalog for Australian broadband seismic stations

K. Tarumi[1,*] and K. Yoshizawa[1,2]

[1] Department of Natural History Sciences, Graduate School of Science, Hokkaido University, Sapporo 060-0810, Japan
[2]Department of Earth & Planetary Sciences, Faculty of Science, Hokkaido University, Sapporo 060-0810, Japan.
[*]Corresponding author: tarumi.kotaro.jp@gmail.com

Supplementary Material 1 (this file) includes additional supporting figures (Figures S1-S9) referred to in the main text. The station orientation catalogs for permanent and temporary stations are summarized separately in Supplementary Materials 2 (a separate PDF file), which includes detailed summary tables of our polarization analysis. As demonstrated in the main text, the station orientation depends on the observation period, so we identified the timing of temporal changes by visually checking the time series of P-wave polarization data for each station. The start and end times indicate the initial and final dates for estimating the median angles. Following is a summary of the contents of Supplementary Materials.

- Figures S1–S5: Summary of time-dependent station orientation and the corresponding standard errors. Figures S1 and S2 show the results for permanent stations except for the *S1* network, Figures S3 and S4 for temporary stations, and Figure S5 for the *S1* network.

- Figure S6: An example of three-component P waveforms with or without the correction for horizontal misorientation at the AU.STKA station.

- Figure S7: A map projection of station misorientations from the geographic north for the *S1* network stations.

- Figure S8: Examples of P-wave receiver functions at AU.STKA using the eastern seismic events.

- Figure S9: Examples of P-wave receiver functions at AU.STKA using the western seismic events.

Note that Supplementary Material 2 (another PDF) includes the station orientation catalog (Tables S1–S3).

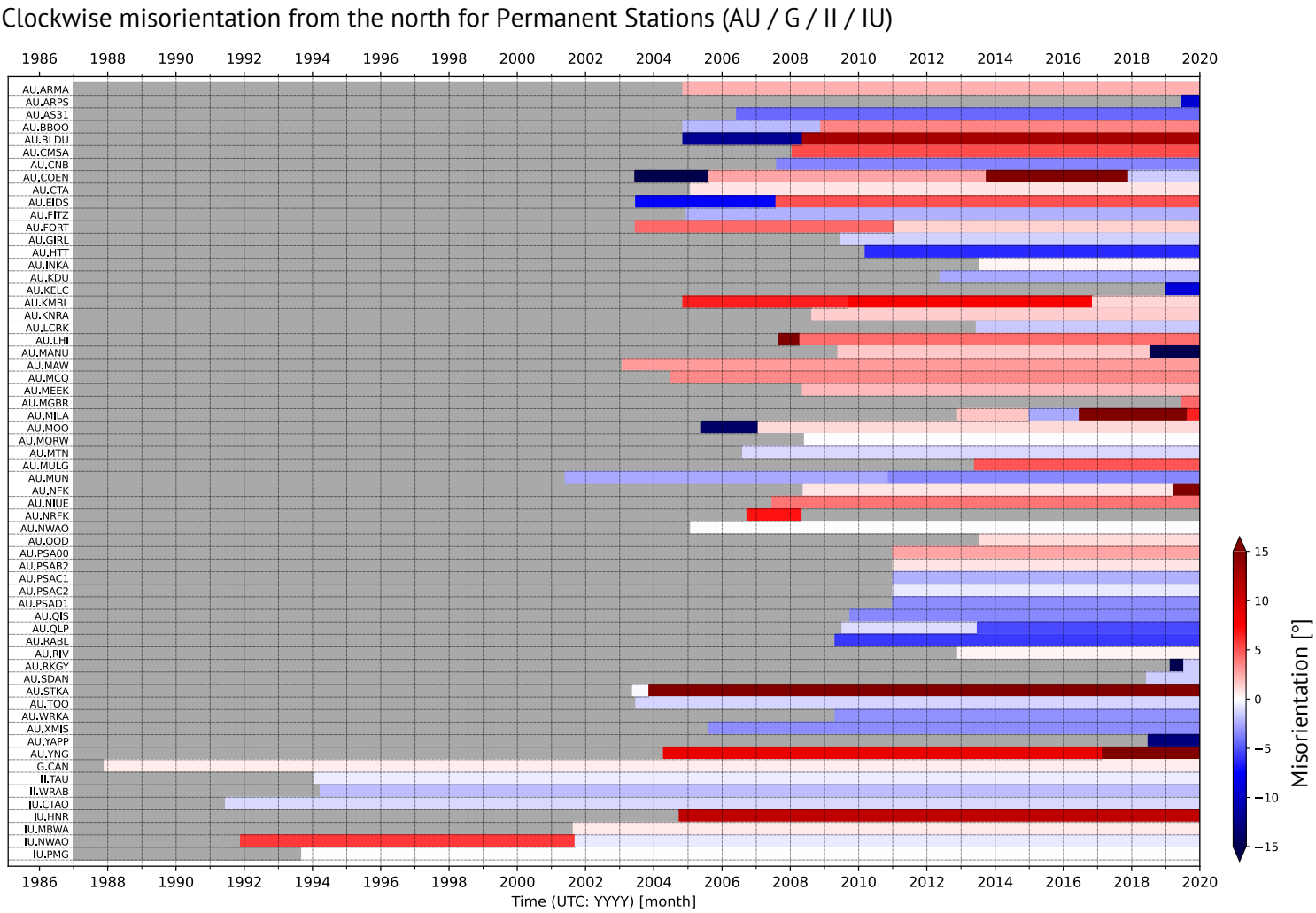

Figure S1. Summary of clockwise misorientation from the geographic north for permanent stations (except for the *S1* network). A positive misorientation value represents the eastward rotation of horizontal sensors from the north. The gray region represents the period when the seismic station has not been operated. Note the operation periods for some stations (AU.ARPS, AU.KELC, AU.MGBR, AU.RKGY, and AU.SDAN) are too short to estimate the proper misorientation in our polarization analysis; see Supplementary Material 2 for details.

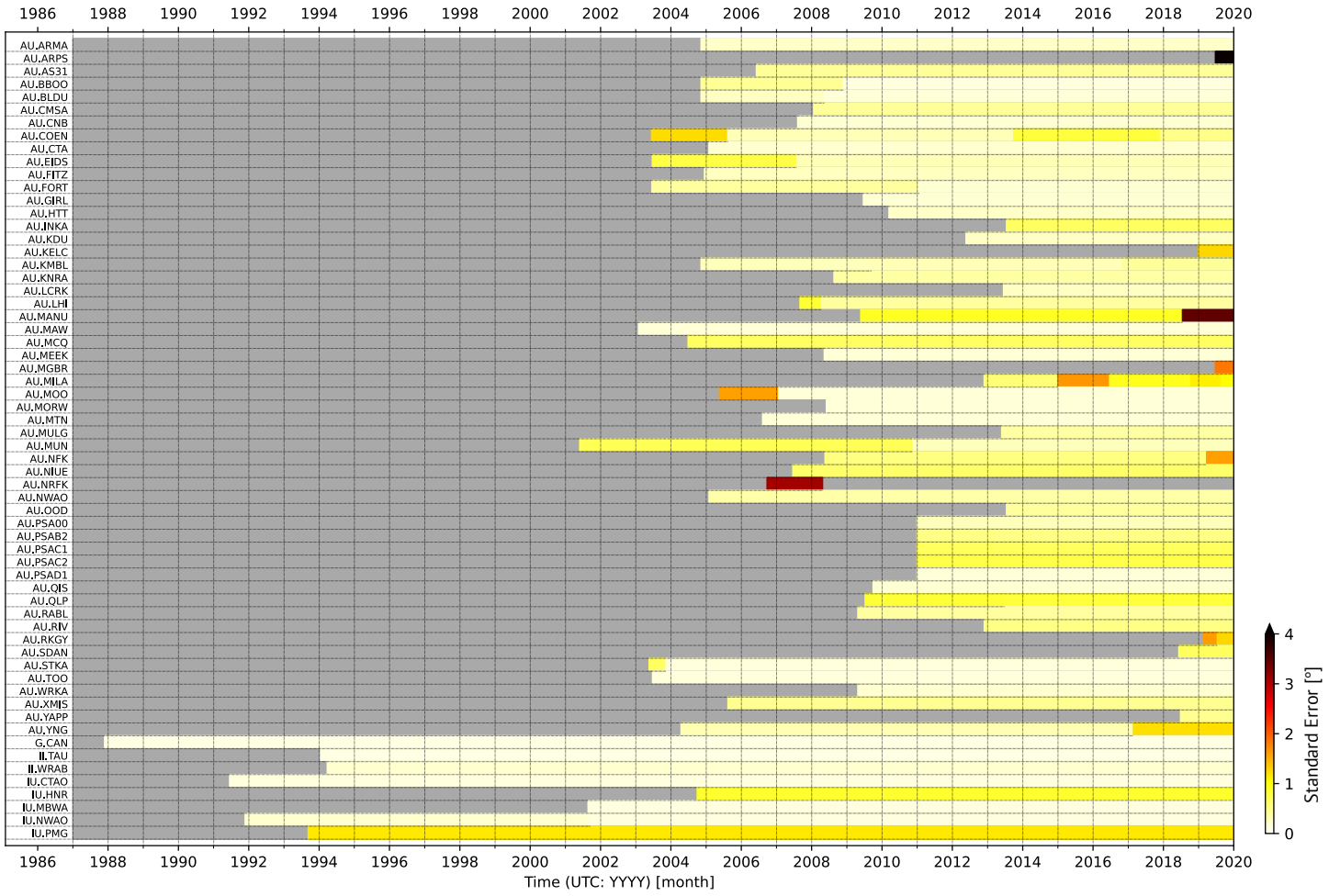

Figure S2. Same as Figure S1, but the summary of standard errors for the estimated misorientation values.

Clockwise misorientation from the north for Temporary stations

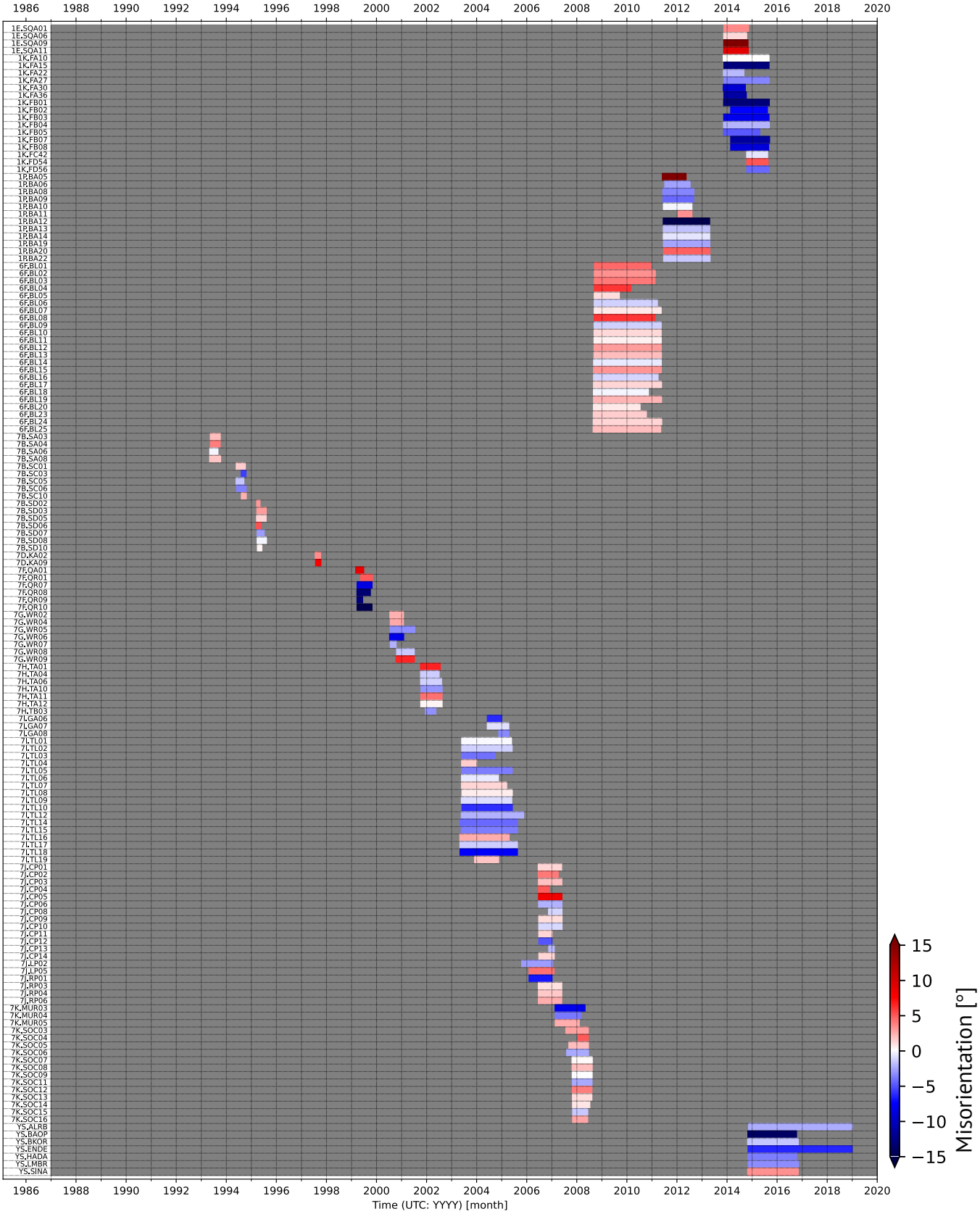

Figure S3: Same as Figure S1, but for the temporary stations.

Standard errors of misorientation values for Temporary stations

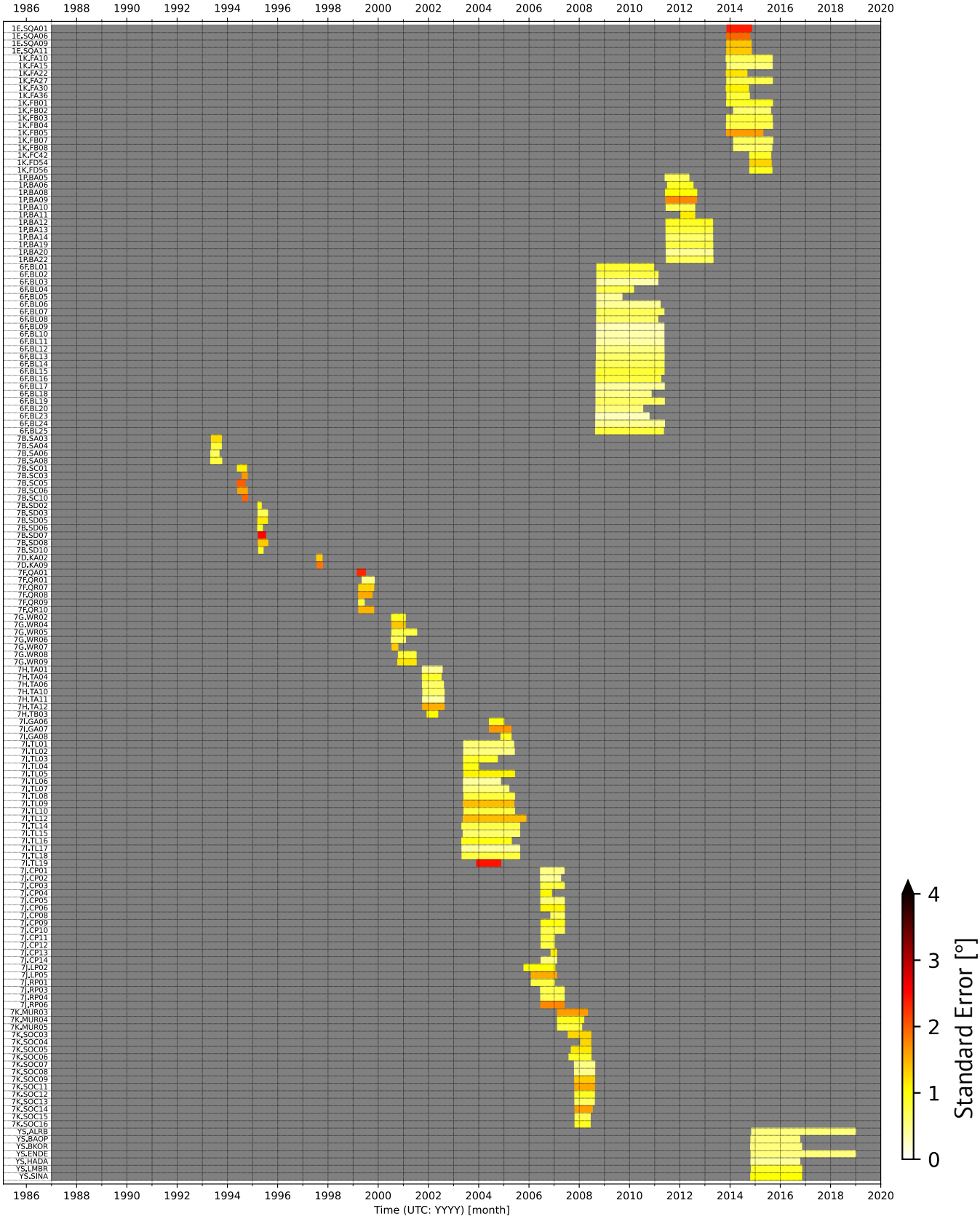

Figure S4: Same as Figure S2, but for the temporary stations.

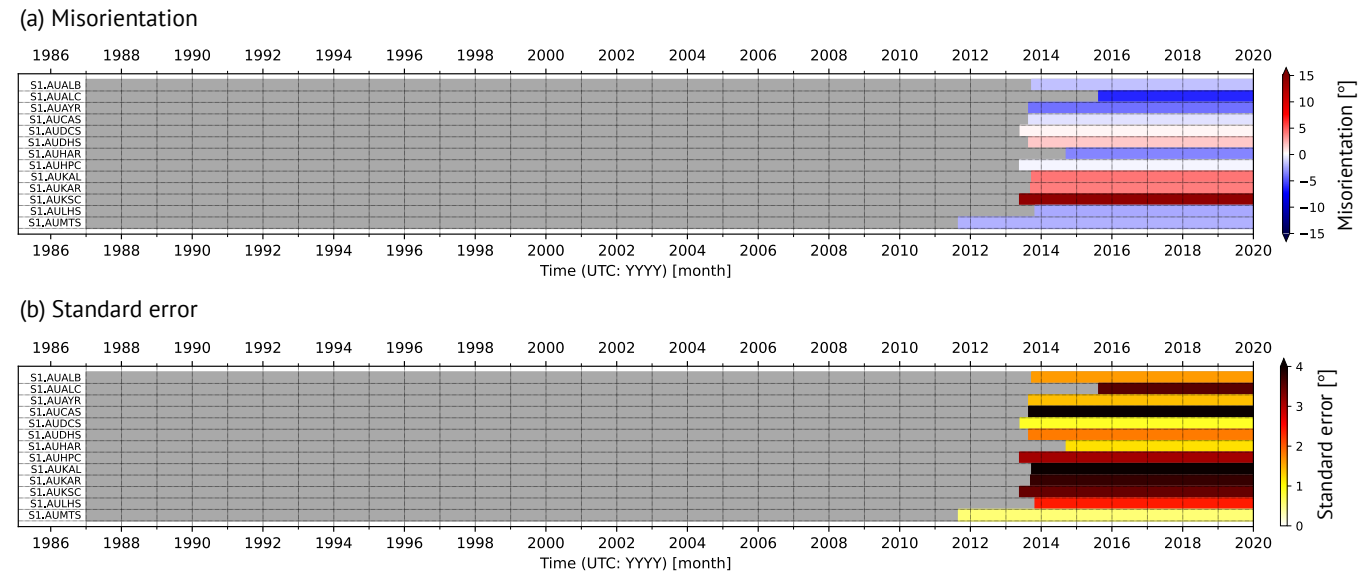

Figure S5: Summary of the *S1* network stations. (a) and (b) are the same as Figures S1 and S2, respectively, but for the *S1* network.

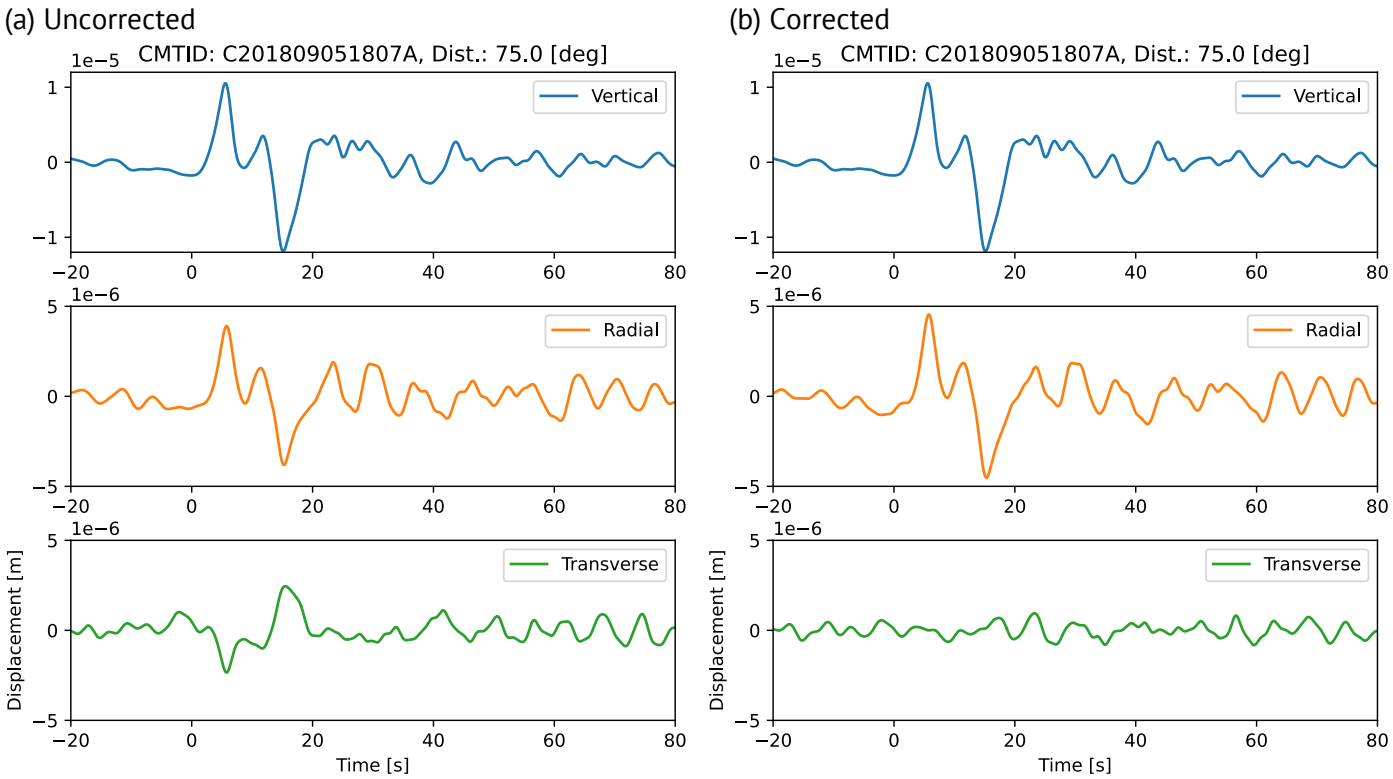

Figure S6: An example of teleseismic P-wave at AU.STKA for a seismic event (Mw 6.6) in Hokkaido, Japan, on September 5, 2018 (UTC). Three-component seismograms (a) before the correction of the station misorientation, and (b) after the correction. Blue, orange, and green lines indicate the vertical, radial, and transverse components. For the uncorrected waveforms in (a), we used the horizontal orientation reported by IRIS/AusPass, while for (b), we employed our new catalog of misorientation. Note that the amplitude scale in the top panel (vertical) is different from the other two horizontal components.

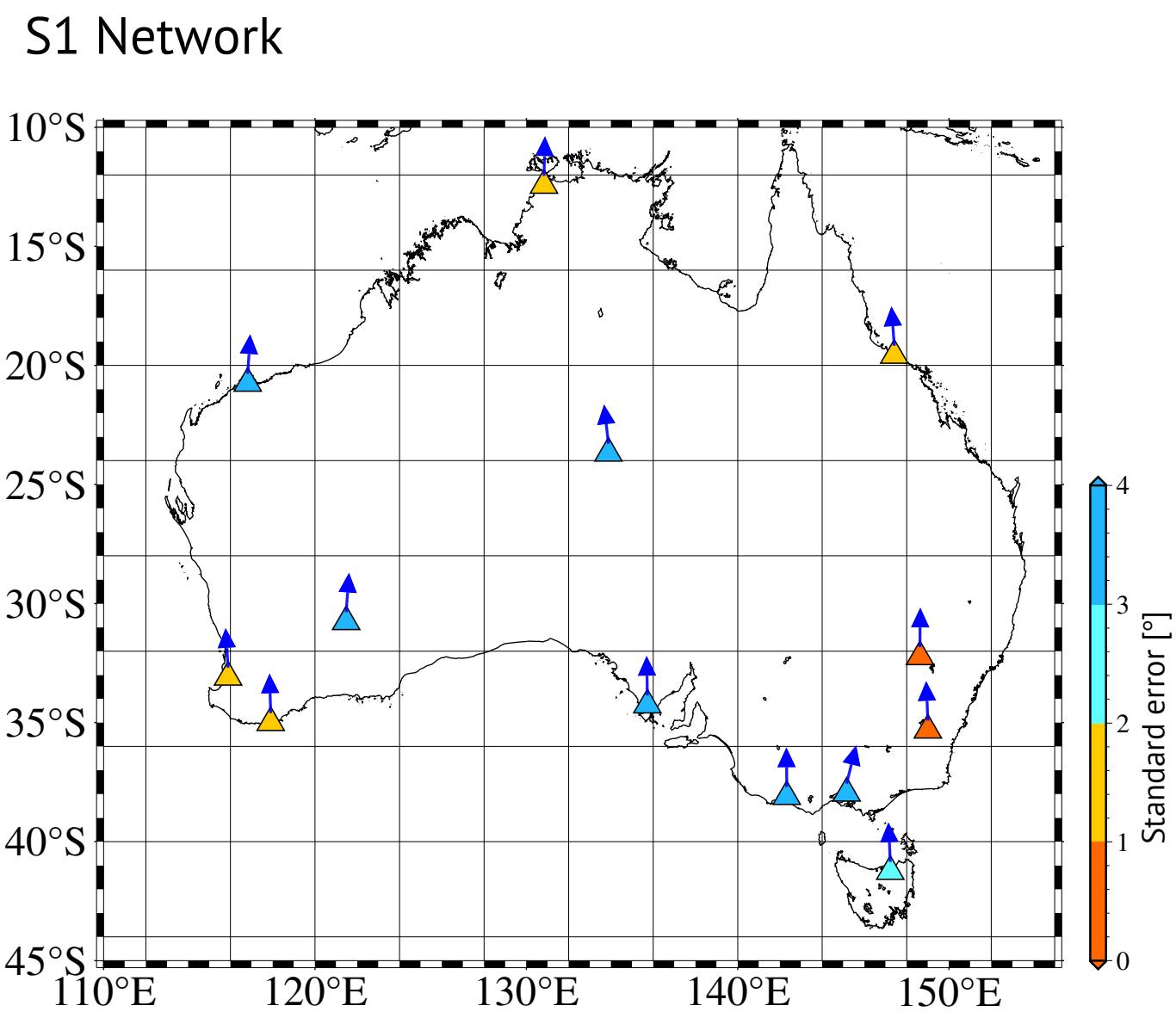

Figure S7: Same as Figures 4 (a-e) and 5 in the main text, but for the *S1* network.

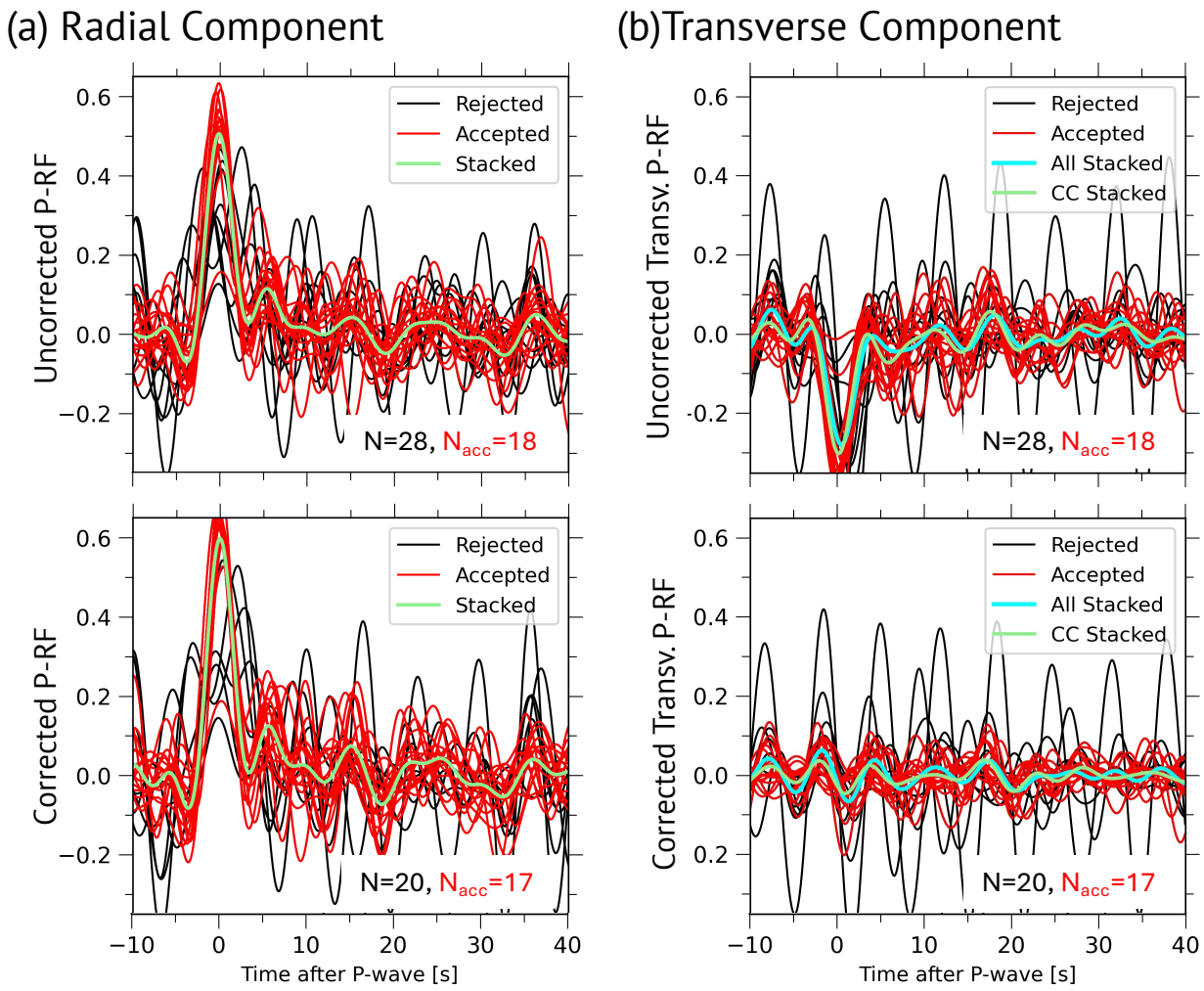

Figure S8: Examples of individual and stacked traces of P-wave receiver functions from the eastern event groups at AU.STKA shown in Figure 5. (a) P-RFs in radial component and (b) transverse component; (top) without and (bottom) with a correction for the station misorientation. Black and red lines are the rejected and accepted traces, respectively, through the cross-correlation-based selection step explained in the main text. Green traces represent the stacked traces, shown as the blue or orange line in Figure 5b.

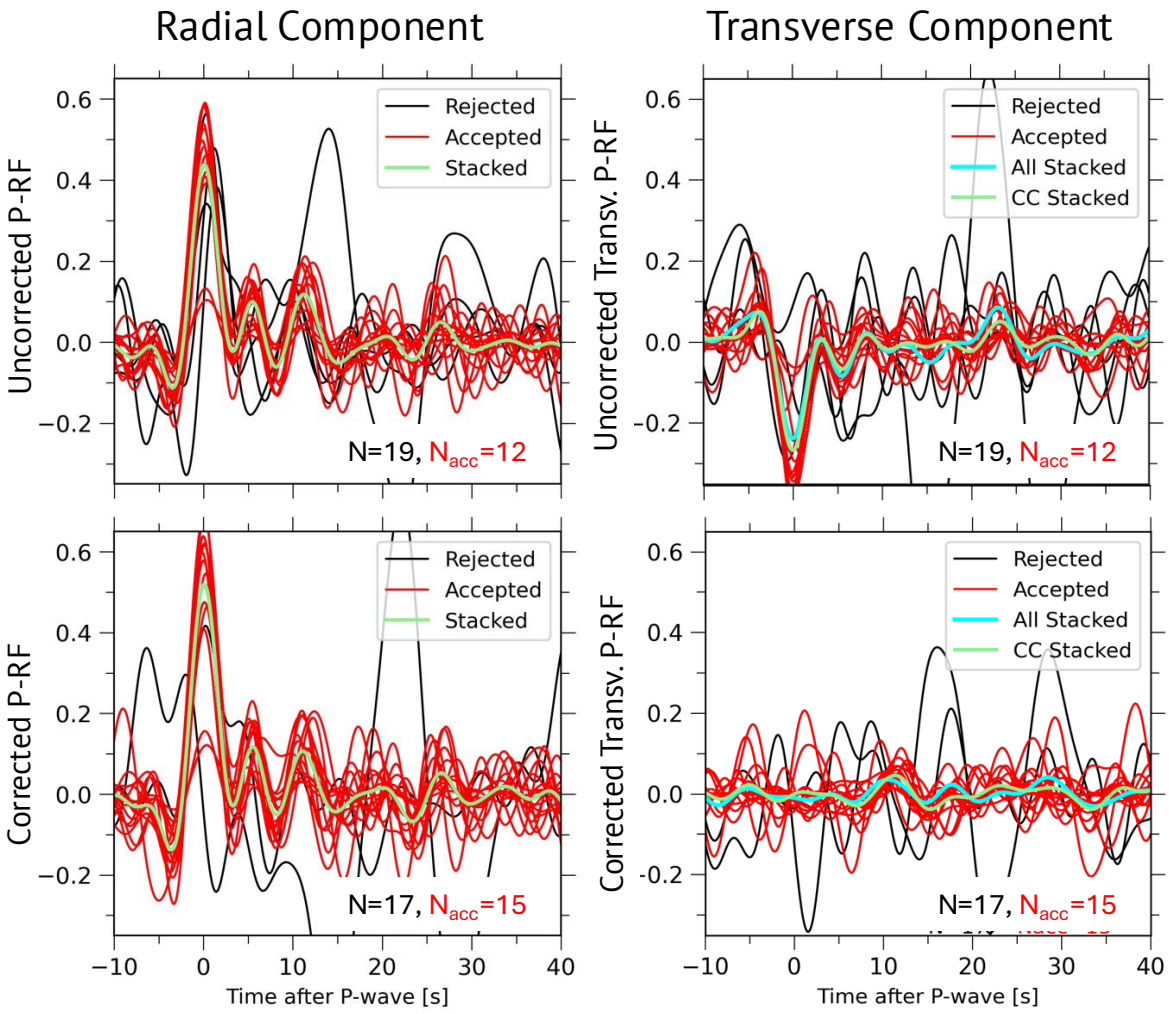

Figure S9: Same as Figure S8, but the P-wave receiver functions from the western event groups.